Applied Surface Science 675 (2024) 160977

Contents lists available at ScienceDirect

Applied Surface Science

journal homepage: www.elsevier.com/locate/apsusc

Full Length Article

Nanosecond laser structuring for enhanced pool boiling performance of SiC surfaces

Hakgae Kim [a,b], Euibeen Jung [b,c], Changyoung Ryu [a,b], Hyoungsoon Lee [b,c,*], Jung Bin In [a,b,*]

[a] Soft Energy Systems and Laser Applications Laboratory, School of Mechanical Engineering, Chung-Ang University, Seoul 06974, Republic of Korea
[b] Department of Intelligent Energy and Industry, Chung-Ang University, Seoul 06974, Republic of Korea
[c] Advanced Thermal Systems Laboratory, School of Mechanical Engineering, Chung-Ang University, Seoul 06974, Republic of Korea

ARTICLE INFO

Keywords:
Laser structuring
Pool boiling
Immersed heat sink
Thermal management
Bubble nucleation

ABSTRACT

Silicon carbide (SiC), which has a wide bandgap and superior material properties, offers higher efficiency than conventional silicon in high-power and high-frequency semiconductor applications. In this study, the thermal management of SiC devices was explored through direct liquid cooling with laser-structured heat sinks. Pyramid-structured fin arrays were fabricated directly onto SiC substrates via laser structuring, and their boiling heat transfer performance was investigated through pool boiling experiments in a 5 °C subcooled condition. Laser structuring not only enhanced wettability due to oxidation but also facilitated nucleation through the laser-induced crevices. The oxidized surface created by the laser exhibited increased hydrophilicity, with a significant decrease in contact angle from 57° to 0°. In the pool boiling experiments, these crevices played a crucial role in enhancing the heat-transfer coefficient (HTC) at low heat fluxes (5–40 W/cm^2), which promoted nucleation, resulting in the formation of very small and rapid bubbles. At heat fluxes above 180 W/cm^2, the large surface area provided by the height of the fin structures further contributed to enhancing the HTC. The sample with the highest performance enhancement exhibited an 114 % increase in critical heat flux and a remarkable 393 % increase in the HTC compared to before laser structuring.

1. Introduction

Gallium nitride (GaN) high-electron-mobility transistors (HEMTs) are promising devices in high-power communications and radar technologies because of their high power-switching efficiency and strong current-handling capabilities [1,2]. However, they encounter significant self-heating issues as operating power increases, which can degrade their performance reliability and efficiency. Hence, thermal management is required to maintain low operating temperatures [3,4]. Silicon carbide (SiC) is a semiconductor material known for its high thermal conductivity, and it is used to dissipate heat in GaN HEMT devices fabricated in a GaN-on-SiC configuration. An efficient approach that has been proposed for thermal management is direct liquid cooling on the surfaces of device substrates [5]. This approach has prompted recent research into developing heat sinks and cooling techniques for SiC to achieve enhanced cooling performance [6,7].

Boiling heat transfer involves the phase change of the working fluid, and the resulting large latent heat can be exploited for device cooling. Two critical parameters represent the performance of boiling heat transfer: critical heat flux (CHF) and heat-transfer coefficient (HTC). CHF indicates the maximum heat flux at which nucleate boiling occurs. If the heat flux surpasses the CHF, the wall temperature will increase dramatically, causing a transition from nucleate boiling to film boiling. Such high temperatures can immediately destroy or potentially damage the device. HTC is obtained by dividing the heat flux by the superheat temperature. A high HTC enables large heat release at a low wall superheat. In pool boiling, where heat transfer due to latent heat during phase change is predominant, the HTC increases as additional bubbles are generated. A system with a high CHF and HTC can maintain nucleate boiling over a wide range of heat fluxes, efficiently releasing heat at relatively low superheat. Therefore, enhancing these two parameters is crucial for improving the cooling performance in pool boiling [8].

Various surface texturing methods have been used to enhance the pool boiling performance of SiC surfaces. Micromachining using computer numerical control is suitable for surface texturing because of its precision and repeatability [9–11]. However, micromachining on SiC, which exhibits high hardness and brittleness, may result in the formation of microcracks and prolonged processing time [12–14].

* Corresponding authors at: School of Mechanical Engineering, Chung-Ang University, Seoul 06974, Republic of Korea.
E-mail addresses: leeh@cau.ac.kr (H. Lee), jbin@cau.ac.kr (J.B. In).

https://doi.org/10.1016/j.apsusc.2024.160977
Received 5 June 2024; Received in revised form 8 August 2024; Accepted 12 August 2024
Available online 13 August 2024

Furthermore, tool wear during the machining process can increase production costs and decrease overall efficiency [15,16]. Reactive-ion etching (RIE) or chemical etching is suitable for machining brittle materials. Unlike the abovementioned micromachining processes, RIE does not subject the material to high pressure during the machining process, minimizing the risk of fine cracks. It also enables the production of intricate patterns and micromachining through mask utilization [17]. However, the etching process is intricate and time-consuming. It involves several steps: applying a photoresist, using a photomask and photolithography equipment to engrave patterns, performing the actual etching process, and removing the photoresist. Owing to its complexity, the process is susceptible to dust contamination, necessitating a clean-room environment, which can be costly. Furthermore, the chemicals employed in etching are toxic, rendering the process environmentally unfriendly [18,19]. Deposition methods, such as electrochemical deposition or chemical vapor deposition, are commonly employed to enhance the pool boiling performance of surfaces by creating hydrophilic or porous structures [20–22]. The presence of these functional materials enhances wettability and provides favorable conditions for bubble nucleation because of their microscale and nanoscale structures. However, prolonged boiling can lead to structural damage or weakened bonds in these functional materials. Additionally, the process is intricate and time-consuming [23,24].

In terms of structuring SiC, laser texturing offers several advantages over the abovementioned surface-texturing methods. Laser texturing using a galvanometer scanner can swiftly process materials within minutes. Furthermore, programmable patterns can be applied to the surface, and energy can be precisely focused on narrow areas for micro-level precision machining [25–28]. Remarkably, even materials with high hardness and brittleness, such as SiC, can be processed without physical contact, thus overcoming the constraints imposed by mechanical properties [29]. Laser-textured surfaces exhibit increased roughness and become hydrophilic owing to the formation of an oxide layer. These characteristics enhance wettability, provide numerous nucleation sites, and ultimately improve pool boiling performance [30–34].

Numerous studies have been conducted to enhance pool boiling performance through laser texturing. Xu et al. [35] employed a nanosecond laser to create pyramid-shaped fins on a flat copper surface. They then investigated the pool boiling performance using fluorinert electronic liquid as the working fluid. The study revealed that the microstructures/nanostructures created by the laser significantly improved wettability and provided highly favorable conditions for bubble formation, inducing ultrafast jet-flow boiling. Kruse et al. [36] textured the surface of stainless steel and studied its pool boiling performance. Femtosecond laser texturing formed microstructures of varying spacings and heights on the surface, depending on the laser fluence. The researchers analyzed the impact of these microstructures on pool boiling performance. Liu et al. [37] researched the pool boiling performance of silicon wafers processed with a femtosecond laser in FC-72. The textured samples with different laser scan spacings exhibited differences in wettability, which affected the pool boiling performance. Serdyukov et al. [38] employed two different lasers with varying wavelengths to texture silicon surfaces and investigate pool boiling phenomena. The laser treatment resulted in surfaces with distinct characteristics depending on the wavelength used. The researchers also analyzed the pool boiling behavior on each of these modified surfaces. Existing research has revealed that material selection, laser parameters, and scanning variables significantly influence the pool boiling characteristics of surfaces. Owing to the growing demand for efficient thermal management in electronic devices, extensive studies have focused on textured silicon and metal heat sink materials. However, no research has been conducted on laser texturing of SiC and its pool boiling performance despite the potential of SiC as a promising material for electronic devices.

In this study, the laser structuring of SiC wafer surfaces was investigated by analyzing their surface morphology and characteristics. Nanosecond laser structuring was applied to create microstructures in the form of pyramids and crevices on the SiC surfaces. These surface modifications significantly enhanced pool-boiling heat transfer. The factors contributing to this improvement were analyzed based on the experimentally obtained pool boiling curves and high-speed camera observations of bubble behavior.

2. Experimental section

2.1. Laser structuring and characterization

The boiling substrate was fabricated on a SiC wafer (4H, semi-insulating, double side polished, surface-oriented {0001}, thickness: ~525 µm, Shanxi Semisic Crystal Co.). The SiC wafer was cut and structured with a nanosecond fiber laser (pulse duration: ~250 ns, wavelength: 1062 nm, beam quality: M^2 <1.6, SP-050P-A-EP-Z-B-Y, SPI Co.). The laser beam was directed onto the SiC surface via a 2-axis galvanometer scanner (DCB210-Y1HP, Thorlabs) and an F-theta lens (focal length: 163 mm, SL16385-Y1, Thorlabs). The diameter of the focused laser beam was ~70.5 µm. The laser scanning path was programmed using SAMLight software (SCAPS GmbH). The wafer was cut into small pieces (25 × 25 mm^2) using the nanosecond laser at a pulse fluence, scanning speed, and pulse repetition frequency of 26.4 J/cm^2, 100 mm/s, and 50 kHz, respectively. The surfaces of the SiC pieces were roughened using a grinding/polishing machine (Labopol-5, Struers Co.) with diamond grit sandpaper (MD-Piano 80, Struers Co.) at 500 RPM for 5 min. The roughened samples exhibited high optical absorption for the fiber laser, and damage to the opposite side caused by a transmitted laser beam was avoided. The roughened surface was subsequently laser-structured using the nanosecond laser (29.7 J/cm^2, 1500 mm/s, and 50 kHz). The laser scanning pattern parameters for surface structuring are presented in Table 1. The laser-structured sample was ultrasonicated with deionized (DI) water for 10 min before a thin-film heater was patterned.

2.2. Fabrication of the thin-film heater

The thin-film heater was fabricated on the bottom surface (opposite the laser-structured surface) of the SiC sample. First, a dispersion of Ag nanoparticles (AgNPs; diameter: ~50 nm, 10 wt% in isopropyl alcohol (IPA), SNP-050c, NIC Co.) was applied to the bottom surface using a spin coater (SPIN-1200D, MIDAS Co.) for 1 min at 300 RPM. The deposited AgNP layer underwent a two-step process using the same fiber laser, resulting in distinct sintered and cleaned sections. Initially, a portion of the layer was selectively sintered (continuous wave mode, 13 W, and 20 mm/s) to create a 10 × 10 mm^2 serpentine heater. Subsequently, the other unaffected area of the layer was removed through laser ablation using the laser in a nanosecond pulse mode (5.1 J/cm^2, 100 mm/s, and 50 kHz).

2.3. Pool boiling setup

The chamber for the pool boiling experiment consisted of an aluminum body and a transparent polycarbonate window, as illustrated

Table 1
Laser scanning repetitions and dimensions of the laser-structured surface structures.

Sample	Laser scan repetition	Groove width (µm)	Pitch (µm)	Structure height (µm)
P1	10	100	120	40
P2	20	100	120	80
P3	40	100	120	155
P4	60	100	120	220
WP1	20	270	300	95
WP2	40	270	300	190

in Fig. 1. DI water served as the working fluid, and the experiments were conducted under atmospheric pressure. An auxiliary heater capable of delivering up to 1 kW was positioned on the side of the chamber wall to maintain the pool temperature at 95 °C during experiments and to pre-boil the water, thereby minimizing noncondensable gases before the experiments. Vaporized water was condensed on the condensing coil connected to the circulating chiller (HH-35, Jeio Tech) and then returned to the water pool. The boiling sample was loaded at the bottom of the chamber, and the bottom-side heater was powered by a DC power supply (EX 300-12, ODA Technologies). The power supplied to the heater was monitored with LabVIEW software using a data acquisition system (NI cDAQ-9174, National Instruments). Additionally, the temperature of the chamber water was monitored by a K-type thermocouple connected to the data acquisition system. Simultaneously, the heater surface temperature and bubble formation were recorded by a thermal imaging camera (A655sc, FLIR) and a high-speed camera (VEO-710L, Phantom), respectively.

2.4. Data analysis

The power supplied to the heater does not entirely reach the surface of the SiC due to heat losses. Because of the high thermal conductivity of SiC, the supplied power on the heater can be dispersed into lateral direction of substrate. Additionally, heat can be dissipated through natural convection and radiation. The effective heat flux, HTC, and superheat regarding these heat losses were numerically calculated using commercial finite element analysis software (COMSOL Multiphysics 6.2). The power measured by the data acquisition system was used as a boundary condition, and the HTC value was iteratively adjusted until the simulated temperature distribution on the heater surface matched the experimental data [39]. The boundary conditions and material properties used in the calculations can be found in Figure S4 and Table S2 of the *Supporting Information*.

The uncertainty of the power supply was ±0.1 % in current and voltage, the uncertainty from the voltage divider was ±1 % for current and ±0.1 % for voltage, the uncertainty of the vernier calipers used was ±0.03 mm, and the uncertainty of the IR camera was ±2 K. The uncertainties of the input heat flux and HTC were calculated using the error propagation method proposed by Coleman and Steele [40]:

$$\frac{\Delta q}{q} = \sqrt{\left(\frac{\Delta I}{I}\right)^2 + \left(\frac{\Delta V}{V}\right)^2 + \left(\frac{\Delta A}{A}\right)^2} \tag{1}$$

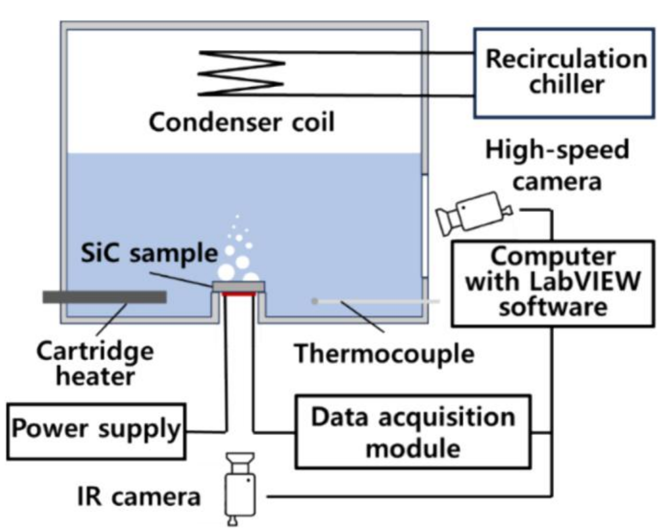

Fig. 1. Schematic of the pool boiling setup.

$$\frac{\Delta h}{h} = \sqrt{\left(\frac{\Delta q}{q}\right)^2 + \left(\frac{\Delta T_w}{T_w - T_{sat}}\right)^2 + \left(\frac{\Delta T_{sat}}{T_w - T_{sat}}\right)^2} \tag{2}$$

The accumulated uncertainty of the input heat flux was ±1.1 %. The uncertainties of the HTC were ±21.4 % at 2.5 W/cm^2 and ±6 % at the CHF.

3. Results and discussion

3.1. Characterization of the laser-structured SiC surfaces

Laser structuring techniques were used to engineer the SiC surface with intersecting grooves that were 100 μm and 270 μm in width and spaced at pitches of 120 μm and 300 μm. Pyramid structures were formed in areas unaffected by the laser, with their heights varying based on the number of laser scans performed. The samples with pyramid structures spaced at 120 μm are denoted by the prefix P, while those with a wider spacing of 300 μm are denoted by WP. Table 1 summarizes the shape of the structures, the width of the grooves, the pitch, and the height of the structures for each sample. Fig. 2 shows the morphology of the structured surface visualized using scanning electron microscopy (SEM; S-3400 N, Hitachi, Japan). Regarding the P3 and P4 samples, where the number of laser scan repetitions was high, the structures lengthened, and crevices were formed where the walls of the structures met at the base. In contrast, regarding the P1, WP1, and WP2 samples, where the number of repetitions was insufficiently high, the grooves were wide, resulting in ample space between the walls of the pyramid structures and a smooth bottom. Thus, no crevices were formed. Regarding the P2 sample, crevices were formed at locations where the grooves overlapped even though there was sufficient space between the structures. The surface structure became rough when melted materials were deposited on it during laser structuring, creating favorable conditions for nucleation. The surface structure also became hydrophilic when coated with an oxidized material during laser structuring.

As indicated in Fig. 3a and Table 2, the investigation of the surface chemistry using X-ray photoelectron spectroscopy (XPS; K-Alpha+, Thermo Fisher Scientific) revealed that the laser-structured surfaces had a higher oxygen ratio than the pristine wafer. Furthermore, the water contact angle decreased, confirming the hydrophilicity of the surface, as shown in Fig. 3b. The hydrophilicity was maintained even after the completion of boiling experiment. For further investigation of the chemical modifications induced by laser structuring, the high-resolution C 1s XPS spectra were obtained from pristine SiC and P3 samples (Fig. 4a and b). The C 1s spectrum of pristine SiC was deconvoluted into three distinct peaks of C–Si (282.4–282.5 eV), C–C (284.8 eV) and C–O (286.1 eV). For the P3 sample, deconvolution revealed the existence of three peaks, corresponding to C–C, C–O, and C=O (287.5 eV) [41–43]. Likewise, the high-resolution Si 2p XPS spectra were obtained from pristine SiC and P3 samples (Fig. 4c and d). Their deconvolutions show Si–C 3/2p (100.3 eV), Si–C 1/2p (100.9 eV), Si–C–O/Si–O (101.5 eV), and Si–O–C 1/2p (102.1 eV) peaks for the pristine SiC; and Si–C–O/Si–O, and Si–O–Si (104.5 eV) for the sample P3 [41–45]. The above result elucidates significant oxidation of surface Si by laser ablation, which contributes to the enhanced hydrophilicity of the modified surface. After laser structuring, new peaks corresponding to C=O, and Si–O–Si bonds emerged, whereas the crystalline bonds between Si and C of pristine SiC almost disappeared near the surface. Energy-dispersive X-ray spectroscopy (EDS) analysis was additionally conducted to confirm the introduction of abundant oxygen elements, and the result is available in the *Supporting Information*.

3.2. HTC enhancement of the SiC surfaces

The CHF of the pristine surface was estimated to validate the reliability of the pool boiling experiments using Kandlikar's model [46]:

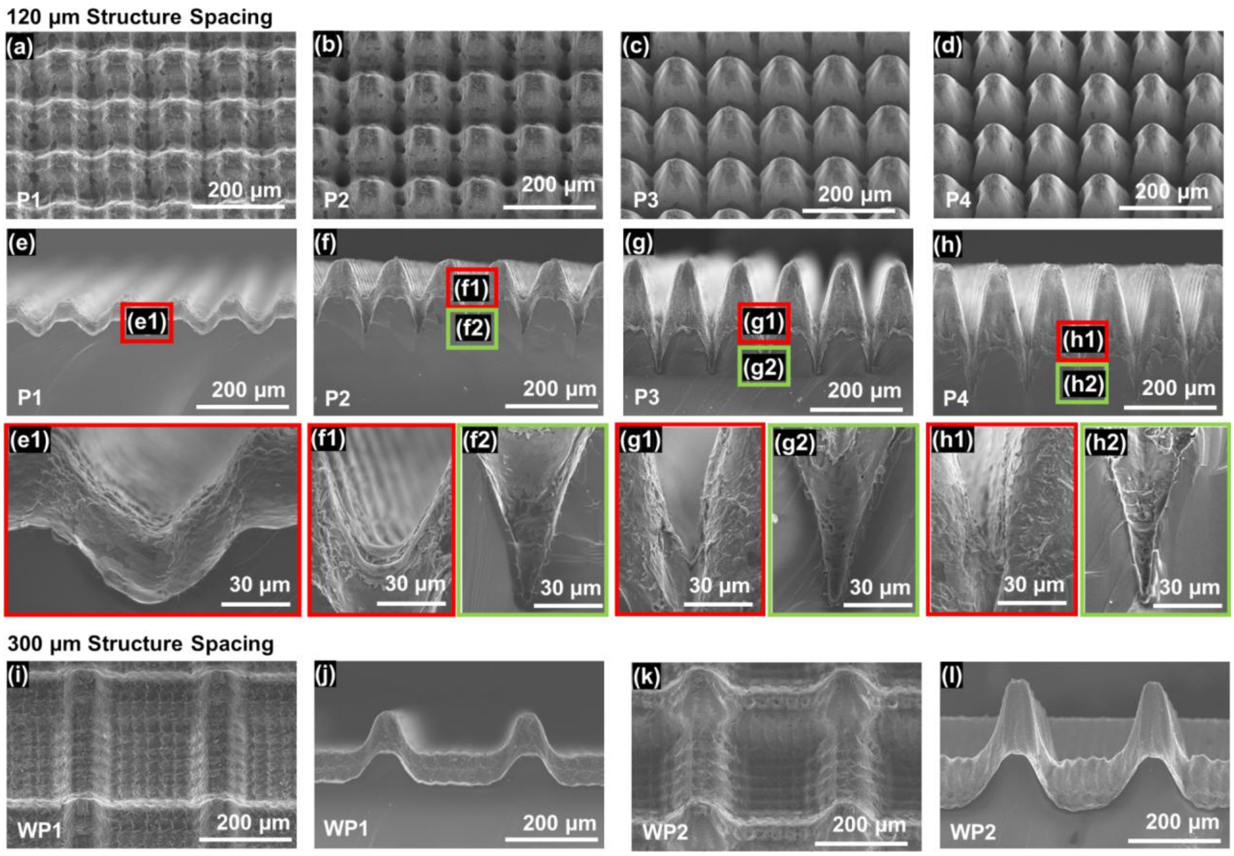

Fig. 2. SEM images of the laser-structured SiC surfaces: (a–d) Top view, (e–h) side view, and (e1, f1–2, g1–2, h1–2) morphologies between the structures of the samples with 120 μm structure spacing. (i, k) Top-view and (j, l) side-view images of the samples with 300 μm structure spacing.

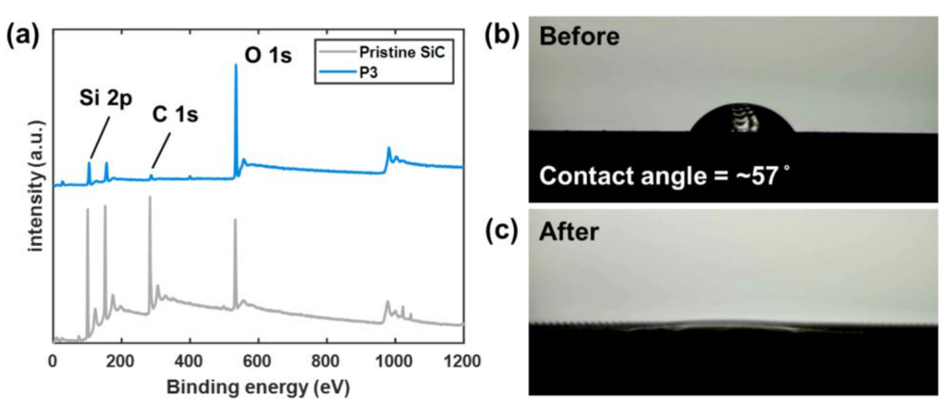

Fig. 3. (a) Full-scan XPS survey spectra of the pristine and P3 samples. Images of the contact angle (b) before and (c) after laser structuring.

Table 2
Surface atomic composition of the major elements in pristine SiC and P3 samples.

Sample	Atomic ratio (%)		
	O 1s	Si 2p	C 1s
Pristine SiC	15.05	42.66	42.29
P3	55.86	34.5	9.64

$$q_c = h_{fg}\rho_v^{\frac{1}{2}}\left(\frac{1+cos\beta}{16}\right)\left[\frac{2}{\pi}+\frac{\pi}{4}(1+cos\beta)cos\phi\right]^{\frac{1}{2}}\times[\sigma g(\rho_L-\rho_v)]^{\frac{1}{4}} \tag{3}$$

where h_{fg}, ρ_L, ρ_v, σ, and g are the latent heat of vaporization, density of the liquid, density of vapor, surface tension of water at 100 ℃, and gravitational acceleration, respectively. Additionally, β and ϕ are the contact angle and inclination of the heater surface, respectively. The predicted CHF of the pristine surface was 111 W/cm^2, which is in close agreement with the value measured in the experiments (118.5 W/cm^2), within a 10 % error. This result demonstrates that the experiment was conducted within a valid setup and was consistent with theoretical predictions.

Fig. 5a and b present the pool boiling curves and HTC of the 120 μm

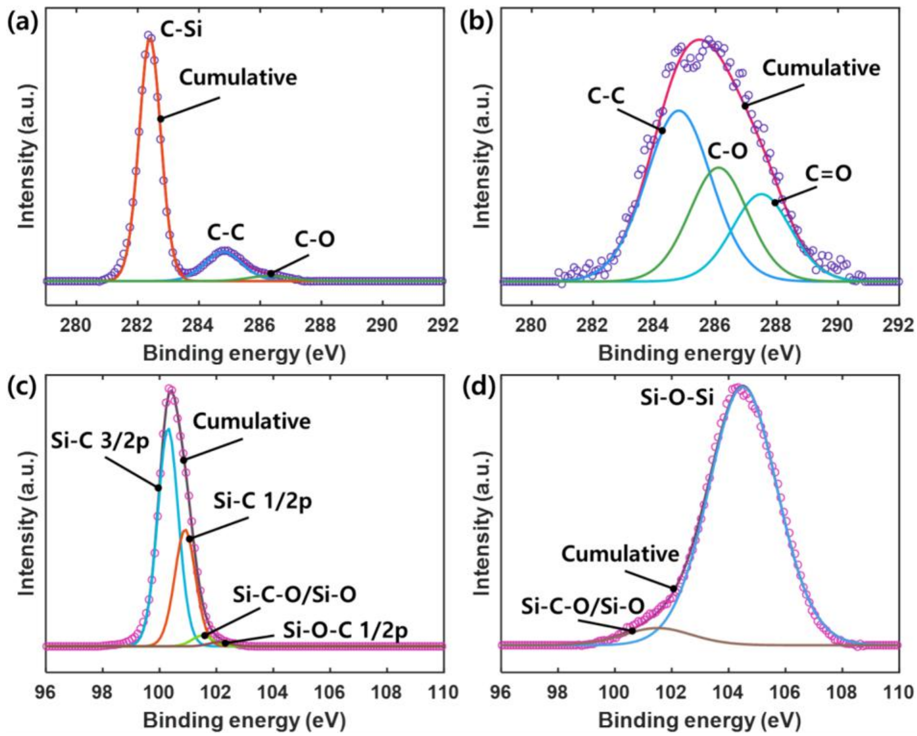

Fig. 4. High-resolution C 1s XPS spectra of (a) pristine SiC and (b) P3 samples. High-resolution Si 2p XPS spectra of (c) pristine SiC and (d) P3 samples.

pitch samples (P1–P4), respectively. They show a trend of increasing HTC with increasing laser ablation depth. Specifically, P4 exhibited ~114 % and ~393 % increases in CHF and HTC, respectively, when compared to the pristine sample. WP1 and WP2 are characterized by fin stuctures without deep crevices, only differing in surface area. The results of the pool boiling experiments for these samples (Fig. 5c and d) demonstrate the impact of surface area on enhancing the HTC. Both samples were found to exhibit similar superheat levels at heat fluxes of 5–40 W/cm^2. This observation reconfirms that crevices caused the variations in superheat within the 5–40 W/cm^2 range. The WP2 sample, which had a relatively large surface area, exhibited a relatively low superheat level at heat fluxes above 40 W/cm^2. Furthermore, this disparity increased as the heat flux increased. It was observed that increasing the heat flux on the laser-structured surface caused additional nucleation sites to be activated, which promoted HTC enhancement in the samples with large surface areas. Fig. 5e displays the HTC at 25–35 W/cm^2. The samples without crevices, namely, WP1, WP2, and P1, all had similarly low HTC values, whereas the other samples exhibited an increase in HTC as the depth of the crevices increased. The maximum HTC value for P4 was found to exceed 180 kW/m^2·K. All the laser-structured samples exhibited an improvement in CHF when compared to the pristine sample. It can be concluded that the hydrophilic surface created by the bonding of oxygen played a role in delaying the CHF. The P4 sample exhibited the highest CHF (~254 W/cm^2) among the samples examined.

The bubble behavior on the laser-structured surface was investigated using a high-speed camera. Fig. 6 presents the results of the bubble dynamics for the pristine, P1, and P4 samples at 6–8 W/cm^2. The bubble departure diameter and frequency of the P1 sample were ~1.3 mm and ~84.5 Hz, respectively, which were 31.5 % lower and 83 % higher than those of the pristine sample (~1.9 mm and ~46 Hz), respectively. Although the P1 sample did not exhibit an increase in HTC, the bubble behavior it exhibited resembled those observed on surfaces where the HTC had been enhanced via laser texturing [36,47]. According to Kruse et al. [48], the oxide layer formed by a laser can function as an insulating layer, resulting in increased superheat during pool boiling. In this study, it was observed that the oxide layer formed by the laser on the SiC surface also acted as an insulating layer, failing to enhance the HTC. The P4 sample had a bubble departure diameter and frequency of 0.3 mm and ~976 Hz, respectively, which were 80 % lower and 11-fold higher than those of the P1 sample, respectively. Notably, the bubble formation cycle in the P4 sample was exceptionally rapid, with some nucleation sites exhibiting vapor columns. Rapid nucleation within cavities can be explained by the classical nucleation theory. Studies employing this nucleation theory to predict the nucleation rate within heterogeneous conical cavity structures have indicated that the nucleation rate increases as the cavity angle decreases [49–51]. The exceptionally high bubble nucleation rate observed in P4 is consistent with the classical nucleation theory, reinforcing its validity. Despite the oxide layer in the P4 sample acting as an insulating barrier, the rapid bubble formation caused by the surface structure influenced HTC enhancement [35].

Fig. 7 displays the bubble behavior of the P1 and P4 samples as the heat flux increases. At a heat flux of 25–35 W/cm^2, P1 and P4 exhibited distinct bubble shapes due to the presence of crevices. Notably, the boiling curve of P4 highlights the significant influence of crevices in reducing superheat within the 5–40 W/cm^2 range, indicating rapid fine bubble formation. As the heat flux increased to 60–75 W/cm^2, bubbles coalesced from the center in both P1 and P4, initiating the formation of vapor columns. During this stage, while crevices continued to play a role, variations in the surface area resulted in noticeable differences in superheat. At a heat flux of 160–190 W/cm^2, vapor columns spanned the entire surface of both P1 and P4. At this stage, the reduction in superheat was influenced by the differences in the surface area. The laser-induced crevices mainly increased the HTC in the low heat flux range of 5–40 W/cm^2, while the large surface area primarily contributed to increasing the HTC at high heat fluxes above 180 W/cm^2.

4. Conclusions

In this study, an array of pyramid-shaped fin structures was formed on a SiC surface using a nanosecond fiber laser to fabricate embedded SiC heat sinks. The laser was operated at a pulse fluence of 29.7 J/cm^2, a

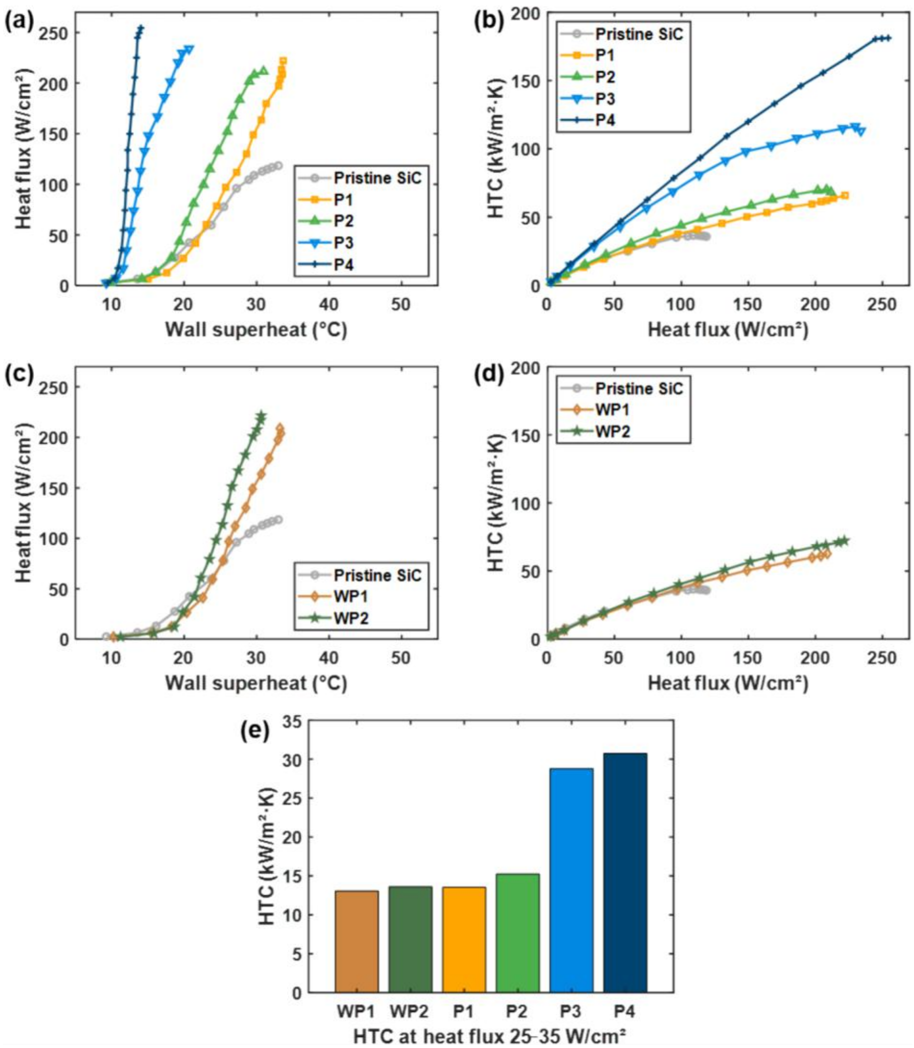

Fig. 5. (a) Pool boiling curves and (b) HTC versus heat flux for the 120 μm pitch samples. (c) Pool boiling curves and (d) HTC versus heat flux for the 300 μm pitch samples. (e) HTCs of the laser-structured samples at 25–35 W/cm^2.

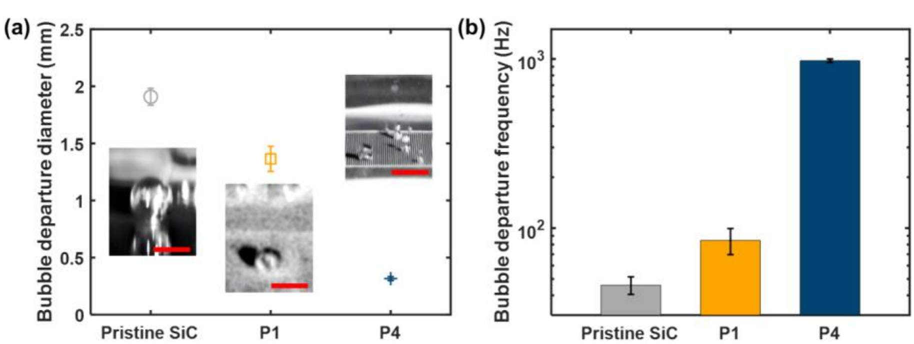

Fig. 6. Bubble behavior on the SiC surfaces at 6–8 W/cm^2: (a) Average bubble departure diameter and bubble images with red scale bars representing 2 mm. (b) Average bubble departure frequency. Error bars in the figures indicate 95 % confidence intervals. (For interpretation of the references to colour in this figure legend, the reader is referred to the web version of this article.)

scanning speed of 1500 mm/s, and a pulse repetition frequency of 50 kHz. The scanning repetition was progressively increased to vary the height of the fin structures. At high scanning repetitions (40 and 60 times), cavities and crevices were created between the fins. XPS analysis of the surface chemistry revealed that the oxygen ratio increased more than threefold, and the hydrophilicity of the oxide layer was confirmed by a decrease in the contact angle (from 57° to 0°). Factors influencing boiling performance were investigated through pool boiling experiments. It was discovered that crevices increased the HTC at low heat fluxes of 5–40 W/cm^2. Moreover, the P4 sample, which contained crevices, exhibited an 80 % decrease in bubble diameter and a 11-fold increase in frequency, when compared to the sample without crevices (P1). This resulted in the formation of very small and rapid bubbles. The rapid nucleation rate in the crevices aligned with the classical nucleation

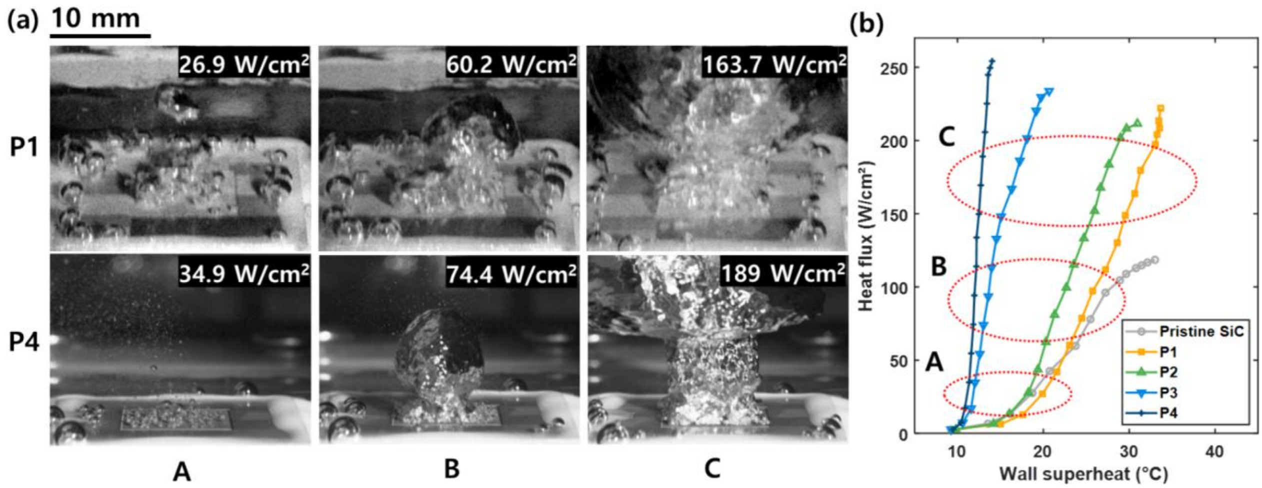

Fig. 7. (a) Boiling behavior on P1 and P4 surfaces at various heat fluxes. (b) Pool boiling curves for the P1–P4 samples.

theory, which states that nucleation rates increase as the angle of conical cavities decreases. The large surface area of the structures was observed to increase the HTC at high heat fluxes exceeding 180 W/cm^2. The surface area effect became apparent as bubbles coalesced to form vapor columns. Although the oxide layer formed by the laser acted as an insulating barrier and hindered HTC enhancement, the reduction in contact angle due to increased hydrophilicity enhanced the CHF. The most remarkable improvement in pool boiling performance was observed in the sample with the highest fin structures and most crevices formed due to high laser repetition rates, where the CHF and HTC increased by 114 % and 393 %, respectively. Further research is required to investigate the long-term durability of boiling performance on SiC surfaces in a continuous nucleate boiling state, the improvement in CHF due to differences in surface morphologies, and the underlying mechanisms of these enhancements.

CRediT authorship contribution statement

Hakgae Kim: Writing – original draft, Visualization, Methodology, Investigation, Formal analysis, Conceptualization. **Euibeen Jung:** Validation, Methodology. **Changyoung Ryu:** Formal analysis, Investigation, Software. **Hyoungsoon Lee:** Writing – review & editing, Validation, Supervision, Project administration, Funding acquisition. **Jung Bin In:** Writing – review & editing, Writing – original draft, Supervision, Project administration, Investigation, Funding acquisition, Conceptualization.

Declaration of competing interest

The authors declare that they have no known competing financial interests or personal relationships that could have appeared to influence the work reported in this paper.

Data availability

Data will be made available on request.

Acknowledgments

This research was supported by the National Research Foundation of Korea (NRF) grant funded by the Korea government (MSIT) (No. NRF-2022R1A2C1010296 and RS-2024-00353227). H. Kim appreciates Dr. Daeyoung Kong's advice on uncertainty calculations.

Appendix A. Supplementary material

Supplementary material to this article can be found online at https://doi.org/10.1016/j.apsusc.2024.160977.

References

[1] N. Keshmiri, D. Wang, B. Agrawal, R. Hou, A. Emadi, Current status and future trends of GaN HEMTs in electrified transportation, IEEE Access 8 (2020) 70553–70571, https://doi.org/10.1109/ACCESS.2020.2986972.
[2] J. Millan, P. Godignon, X. Perpina, A. Perez-Tomas, J. Rebollo, A survey of wide bandgap power semiconductor devices, IEEE Trans. Power Electron. 29 (2014) 2155–2163, https://doi.org/10.1109/TPEL.2013.2268900.
[3] G. Agarwal, T. Kazior, T. Kenny, D. Weinstein, Modeling and analysis for thermal management in gallium nitride HEMTs using microfluidic cooling, J. Electron. Packag. 139 (2017) 011001, https://doi.org/10.1115/1.4035064.
[4] Z. Yan, G. Liu, J.M. Khan, A.A. Balandin, Graphene quilts for thermal management of high-power GaN transistors, Nat. Commun. 3 (2012) 827, https://doi.org/10.1038/ncomms1828.
[5] R. Van Erp, R. Soleimanzadeh, L. Nela, G. Kampitsis, E. Matioli, Co-designing electronics with microfluidics for more sustainable cooling, Nature 585 (2020) 211–216, https://doi.org/10.1038/s41586-020-2666-1.
[6] D.G. Bae, R.K. Mandel, S.V. Dessiatoun, S. Rajgopal, S.P. Roberts, M. Mehregany, M.M. Ohadi, Embedded two-phase cooling of high heat flux electronics on silicon carbide (SiC) using thin-film evaporation and an enhanced delivery system (FEEDS) manifold-microchannel cooler, in: In: 2017 16th IEEE Intersociety Conference on Thermal and Thermomechanical Phenomena in Electronic Systems (ITherm), IEEE, Orlando, FL, 2017, pp. 466–472, https://doi.org/10.1109/ITHERM.2017.7992511.
[7] N. Cassada, C. Anderson, L. Kubicek, D. Hobby, C. Frye, S. Baxamusa, J. Kotovsky, K. Jackson, I. Ladner, T. Bandhauer, SiC microchannel heat sinks for high heat flux dissipation of 1 kW/cm ^{2}, IEEE Trans. Compon., Packag. Manufact. Technol. 13 (2023) 655–665, https://doi.org/10.1109/TCPMT.2023.3281772.
[8] M.M. Shah, Two-phase heat transfer, First edition, Wiley, Hoboken, 2021.
[9] M.S. El-Genk, A. Suszko, Effects of inclination angle and liquid subcooling on nucleate boiling on dimpled copper surfaces, Int. J. Heat Mass Transf. 95 (2016) 650–661, https://doi.org/10.1016/j.ijheatmasstransfer.2015.12.048.
[10] D.J. Guckenberger, T.E. De Groot, A.M.D. Wan, D.J. Beebe, E.W.K. Young, Micromilling: a method for ultra-rapid prototyping of plastic microfluidic devices, Lab. Chip. 15 (2015) 2364–2378, https://doi.org/10.1039/C5LC00234F.
[11] D. Deng, L. Chen, W. Wan, T. Fu, X. Huang, Flow boiling performance in pin fin-interconnected reentrant microchannels heat sink in different operational conditions, Appl. Therm. Eng. 150 (2019) 1260–1272, https://doi.org/10.1016/j.applthermaleng.2019.01.092.
[12] T. Zhang, F. Jiang, H. Huang, J. Lu, Y. Wu, Z. Jiang, X. Xu, Towards understanding the brittle–ductile transition in the extreme manufacturing, Int. J. Extrem. Manuf. 3 (2021) 022001, https://doi.org/10.1088/2631-7990/abdfd7.
[13] Z.J. Choong, D. Huo, P. Degenaar, A. O'Neill, Micro-machinability and edge chipping mechanism studies on diamond micro-milling of monocrystalline silicon, J. Manufact. Proc. 38 (2019) 93–103, https://doi.org/10.1016/j.jmapro.2019.01.004.
[14] B.Z. Balázs, N. Geier, M. Takács, J.P. Davim, A review on micro-milling: recent advances and future trends, Int. J. Adv. Manuf. Technol. 112 (2021) 655–684, https://doi.org/10.1007/s00170-020-06445-w.
[15] X. Li, X. Liu, C. Yue, S.Y. Liang, L. Wang, Systematic review on tool breakage monitoring techniques in machining operations, Int. J. Mach. Tools Manuf. 176 (2022) 103882, https://doi.org/10.1016/j.ijmachtools.2022.103882.

[16] J. Dou, S. Jiao, C. Xu, F. Luo, L. Tang, X. Xu, Unsupervised online prediction of tool wear values using force model coefficients in milling, Int. J. Adv. Manuf. Technol. 109 (2020) 1153–1166, https://doi.org/10.1007/s00170-020-05684-1.

[17] Z. Lei, B. Liu, P. Xu, Y. Zhang, J. Wei, The pool boiling heat transfer and critical vapor column coalescence mechanism of block-divided microstructured surfaces, Int. J. Heat Mass Transf. 150 (2020) 119362, https://doi.org/10.1016/j.ijheatmasstransfer.2020.119362.

[18] W.-T. Tsai, H.-P. Chen, W.-Y. Hsien, A review of uses, environmental hazards and recovery/recycle technologies of perfluorocarbons (PFCs) emissions from the semiconductor manufacturing processes, J. Loss Prevent. Proc. Indust. 15 (2002) 65–75, https://doi.org/10.1016/S0950-4230(01)00067-5.

[19] H. Li, Microfabrication techniques for producing freestanding multi-dimensional microstructures, Microsyst. Technol. 22 (2016) 223–237, https://doi.org/10.1007/s00542-015-2720-3.

[20] Z. Yao, Y.-W. Lu, S.G. Kandlikar, Effects of nanowire height on pool boiling performance of water on silicon chips, Int. J. Therm. Sci. 50 (2011) 2084–2090, https://doi.org/10.1016/j.ijthermalsci.2011.06.009.

[21] A. Mehdikhani, H. Moghadasi, H. Saffari, An experimental investigation of pool boiling augmentation using four-step electrodeposited micro/nanostructured porous surface in distilled water, Int. J. Mech. Sci. 187 (2020) 105924, https://doi.org/10.1016/j.ijmecsci.2020.105924.

[22] Z. Cao, B. Liu, C. Preger, Z. Wu, Y. Zhang, X. Wang, M.E. Messing, K. Deppert, J. Wei, B. Sundén, Pool boiling heat transfer of FC-72 on pin-fin silicon surfaces with nanoparticle deposition, Int. J. Heat Mass Transf. 126 (2018) 1019–1033, https://doi.org/10.1016/j.ijheatmasstransfer.2018.05.033.

[23] D. Kong, K. Kim, E. Jung, K. Jiang, Q. Wu, B. Jang, H.-J. Kwon, M. Asheghi, K. E. Goodson, H. Lee, Boiling-induced thermal degradation of copper inverse opals and its mitigation, Int. Commun. Heat Mass Transf. 151 (2024) 107250, https://doi.org/10.1016/j.icheatmasstransfer.2024.107250.

[24] Y. Sun, Y. Tang, S. Zhang, W. Yuan, H. Tang, A review on fabrication and pool boiling enhancement of three-dimensional complex structures, Renew. Sustain. Energy Rev. 162 (2022) 112437, https://doi.org/10.1016/j.rser.2022.112437.

[25] C. Ryu, H.M. Do, J.B. In, Enhanced performance of densified laser-induced graphene supercapacitor electrodes in dimpled polyimide, Appl. Surf. Sci. 643 (2024) 158696, https://doi.org/10.1016/j.apsusc.2023.158696.

[26] M. Može, M. Zupančič, M. Steinbücher, I. Golobič, H. Gjerkeš, Nanosecond laser-textured copper surfaces hydrophobized with self-assembled monolayers for enhanced pool boiling heat transfer, Nanomaterials 12 (2022) 4032, https://doi.org/10.3390/nano12224032.

[27] M. Zupančič, M. Može, P. Gregorčič, I. Golobič, Nanosecond laser texturing of uniformly and non-uniformly wettable micro structured metal surfaces for enhanced boiling heat transfer, Appl. Surf. Sci. 399 (2017) 480–490, https://doi.org/10.1016/j.apsusc.2016.12.120.

[28] A. Hadžić, M. Može, K. Arhar, M. Zupančič, I. Golobič, Effect of nanoparticle size and concentration on pool boiling heat transfer with TiO_2 nanofluids on laser-textured copper surfaces, Nanomaterials 12 (2022) 2611, https://doi.org/10.3390/nano12152611.

[29] C. Wu, X. Fang, F. Liu, X. Guo, R. Maeda, Z. Jiang, High speed and low roughness micromachining of silicon carbide by plasma etching aided femtosecond laser processing, Ceram. Int. 46 (2020) 17896–17902, https://doi.org/10.1016/j.ceramint.2020.04.097.

[30] D. Kong, M. Kang, K.Y. Kim, J. Jang, J. Cho, J.B. In, H. Lee, Hierarchically structured laser-induced graphene for enhanced boiling on flexible substrates, ACS Appl. Mater. Interf. 12 (2020) 37784–37792, https://doi.org/10.1021/acsami.0c11402.

[31] H. Zhou, J. Lee, M. Kang, H. Kim, H. Lee, J.B. In, All laser-based fabrication of microchannel heat sink, Mater. Design 221 (2022) 110968, https://doi.org/10.1016/j.matdes.2022.110968.

[32] S. Lee, Y. Kim, H. Ki, J. Lee, Pool-boiling enhancement on periodic micro/nano ripple-structured surfaces fabricated by femtosecond laser, Int. Commun. Heat Mass Transf. 148 (2023) 107072, https://doi.org/10.1016/j.icheatmasstransfer.2023.107072.

[33] A. Hadžić, M. Može, M. Zupančič, I. Golobič, Superbiphilic laser-microengineered surfaces with a self-assembled monolayer coating for exceptional boiling performance, Adv. Funct. Mater. 34 (2024) 2310662, https://doi.org/10.1002/adfm.202310662.

[34] M. Može, M. Senegačnik, P. Gregorčič, M. Hočevar, M. Zupančič, I. Golobič, Laser-engineered microcavity surfaces with a nanoscale superhydrophobic coating for extreme boiling performance, ACS Appl. Mater. Interf. 12 (2020) 24419–24431, https://doi.org/10.1021/acsami.0c01594.

[35] Z. Xu, P. Zhang, C. Yu, W. Miao, Q. Chang, M. Qiu, Y. Li, Y. Tian, L. Jiang, Liquid-superspreading-boosted high-performance jet-flow boiling for enhancement of phase-change cooling, Adv. Mater. 35 (2023) 2210557, https://doi.org/10.1002/adma.202210557.

[36] C.M. Kruse, T. Anderson, C. Wilson, C. Zuhlke, D. Alexander, G. Gogos, S. Ndao, Enhanced pool-boiling heat transfer and critical heat flux on femtosecond laser processed stainless steel surfaces, Int. J. Heat Mass Transf. 82 (2015) 109–116, https://doi.org/10.1016/j.ijheatmasstransfer.2014.11.023.

[37] B. Liu, J. Liu, Y. Zhang, J. Wei, W. Wang, Experimental and theoretical study of pool boiling heat transfer and its CHF mechanism on femtosecond laser processed surfaces, Int. J. Heat Mass Transf. 132 (2019) 259–270, https://doi.org/10.1016/j.ijheatmasstransfer.2018.12.003.

[38] V. Serdyukov, I. Vladyko, S. Starinskiy, A. Rodionov, Y. Shukhov, I. Malakhov, A. Safonov, A. Surtaev, Pool boiling performance on the textured hemi-wicking surfaces fabricated by nanosecond laser ablation, Appl. Therm. Eng. 228 (2023) 120472, https://doi.org/10.1016/j.applthermaleng.2023.120472.

[39] Y. Song, C.D. Díaz-Marín, L. Zhang, H. Cha, Y. Zhao, E.N. Wang, Three-tier hierarchical structures for extreme pool boiling heat transfer performance, Adv. Mater. 34 (2022) 2200899, https://doi.org/10.1002/adma.202200899.

[40] H.W. Coleman, W.G. Steele, Engineering application of experimental uncertainty analysis, AIAA J. 33 (1995) 1888–1896, https://doi.org/10.2514/3.12742.

[41] W. Guo, X. Kong, M. Wang, S. Zhang, Y. Qiao, Z. Wang, L. Zhou, M. Chen, J. Ma, D. Meng, S. Yang, X. Tang, X. Du, Y. Zhang, Defect-engineered MnO_2 as catalyst for the chemical mechanical polishing of silicon carbide wafer, ECS J. Solid State Sci. Technol. 12 (2023) 074005, https://doi.org/10.1149/2162-8777/ace73d.

[42] S. Zhan, B. Liu, X. Yu, X. Chen, G. Zeng, Y. Zhao, Fabrication of homogeneous nanoporous structure on 4H-/6H-SiC wafer surface via efficient and eco-friendly electrolytic plasma-assisted chemical etching, Small 19 (2023) 2205720, https://doi.org/10.1002/smll.202205720.

[43] M.D. Pirnaci, L. Spitaleri, D. Tenaglia, F. Perricelli, M.E. Fragalà, C. Bongiorno, A. Gulino, Systematic characterization of plasma-etched trenches on 4H-SiC wafers, ACS Omega 6 (2021) 20667–20675, https://doi.org/10.1021/acsomega.1c02905.

[44] S.S. Abbas, G.J. Rees, N.L. Kelly, C.E.J. Dancer, J.V. Hanna, T. McNally, Facile silane functionalization of graphene oxide, Nanoscale 10 (2018) 16231–16242, https://doi.org/10.1039/C8NR04781B.

[45] R. Sharma, P.K. Kar, S. Dash, Correlating solvation-adsorption phenomena of some styrylpyridinium dyes on SDS modified silica surface in organic media, J. Dispersion Sci. Technol. 45 (2024) 548–558, https://doi.org/10.1080/01932691.2022.2161562.

[46] S.G. Kandlikar, A theoretical model to predict pool boiling CHF incorporating effects of contact angle and orientation, J. Heat Transf. 123 (2001) 1071–1079, https://doi.org/10.1115/1.1409265.

[47] V. Serdyukov, S. Starinskiy, I. Malakhov, A. Safonov, A. Surtaev, Laser texturing of silicon surface to enhance nucleate pool boiling heat transfer, Appl. Therm. Eng. 194 (2021) 117102, https://doi.org/10.1016/j.applthermaleng.2021.117102.

[48] C. Kruse, A. Tsubaki, C. Zuhlke, D. Alexander, M. Anderson, E. Peng, J. Shield, S. Ndao, G. Gogos, Influence of copper oxide on femtosecond laser surface processed copper pool boiling heat transfer surfaces, J. Heat Transf. 141 (2019) 051503, https://doi.org/10.1115/1.4043129.

[49] P.M. Wilt, Nucleation rates and bubble stability in water-carbon dioxide solutions, J. Colloid Interf. Sci. 112 (1986) 530–538, https://doi.org/10.1016/0021-9797(86)90122-0.

[50] W. Xu, Z. Lan, B. Peng, R. Wen, X. Ma, Heterogeneous nucleation capability of conical microstructures for water droplets, RSC Adv. 5 (2015) 812–818, https://doi.org/10.1039/C4RA12352B.

[51] S.N. Sahu, A.A. Gokhale, A. Mehra, Numerical prediction of effect of oxide characteristics on heterogeneous nucleation of bubbles in aluminium foaming, Trans. Ind. Inst. Met. 65 (2012) 795–800, https://doi.org/10.1007/s12666-012-0190-1.